Tumor restriction by type I collagen opposes tumor-promoting effects of cancer-associated fibroblasts

Sonakshi Bhattacharjee, Florian Hamberger, Aashreya Ravichandra, Maximilian Miller, Silvia Affo, Ajay Nair, Aveline Filliol, LiKang Chin, Thomas M. Savage, Deqi Yin, Peter A. Sims, Ben Z. Stanger, Kenneth P. Olive, Naita Maren Wirsik, Nicholas Arpaia, Ekihiro Seki, Matthias Mack, Di Zhu, Thomas Schmidt, Rebecca G. Wells, Ingmar Mederacke and Robert F. Schwabe

SUPPLEMENTS FILES

Supplementary Figures S1-11

Supplementary Table S1-S3

Supplementary Methods and References

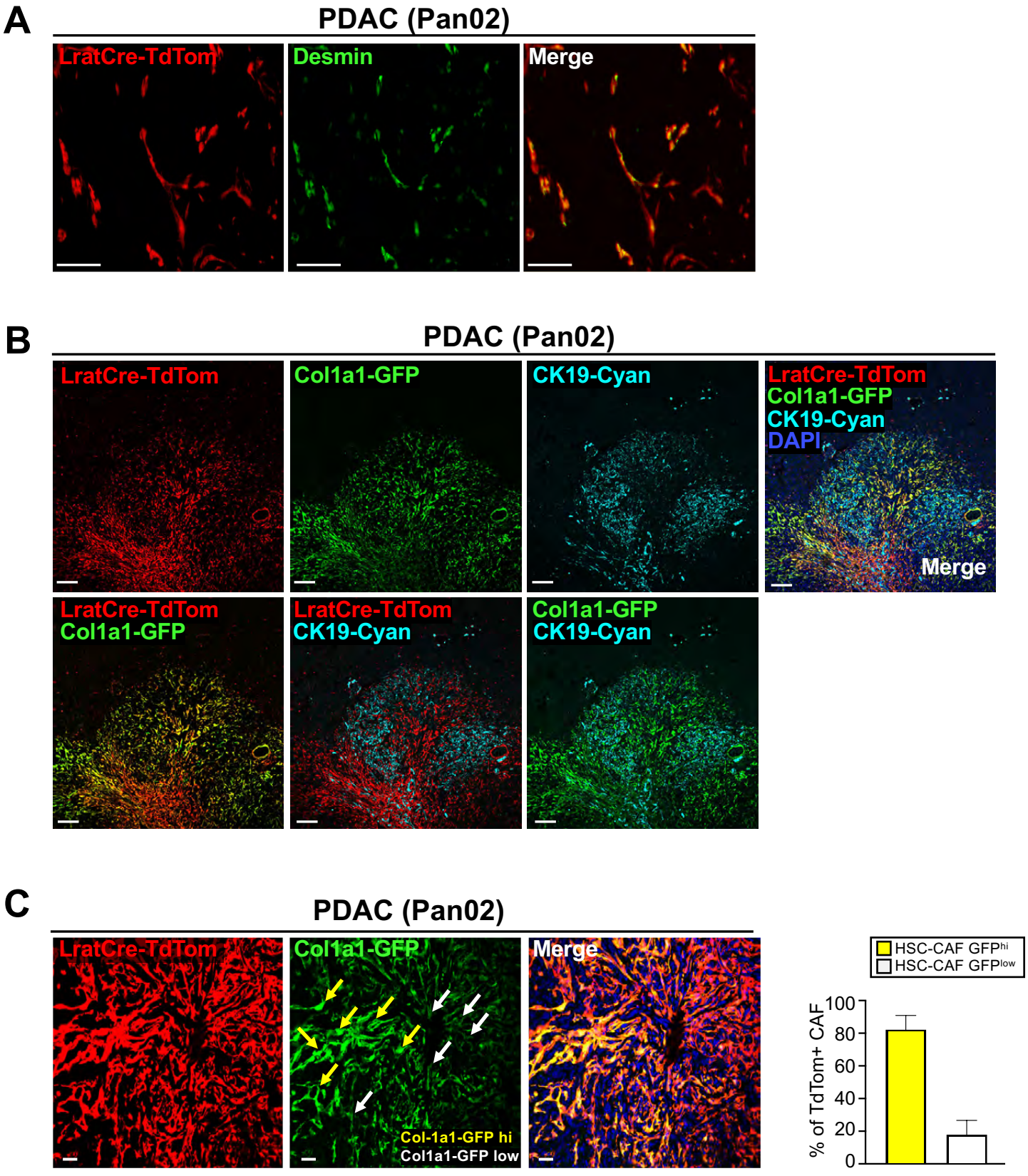

Fig. S1 | Origin and characterization of CAF. A. Representative image showing colocalization of Lrat-TdTomato with HSC marker desmin in Pan02 liver metastasis. Scale bars, 100µm. **B.** Representative image displaying spatial organization of CK19-positive tumor cells with Lrat-TdTomato and Col1a1-GFP positive CAF in PanO2 liver metastasis. Scale bars, 100 µm. **C.** Representative images and quantification from confocal microscopy displaying LratCre-TdTomato and Col1a1-GFP. Col1a1-GFP hi cells are marked with a white arrowhead, Col1a1-GFP low cells are marked with a green arrowhead. n=8, Scale bars, 50 µm.

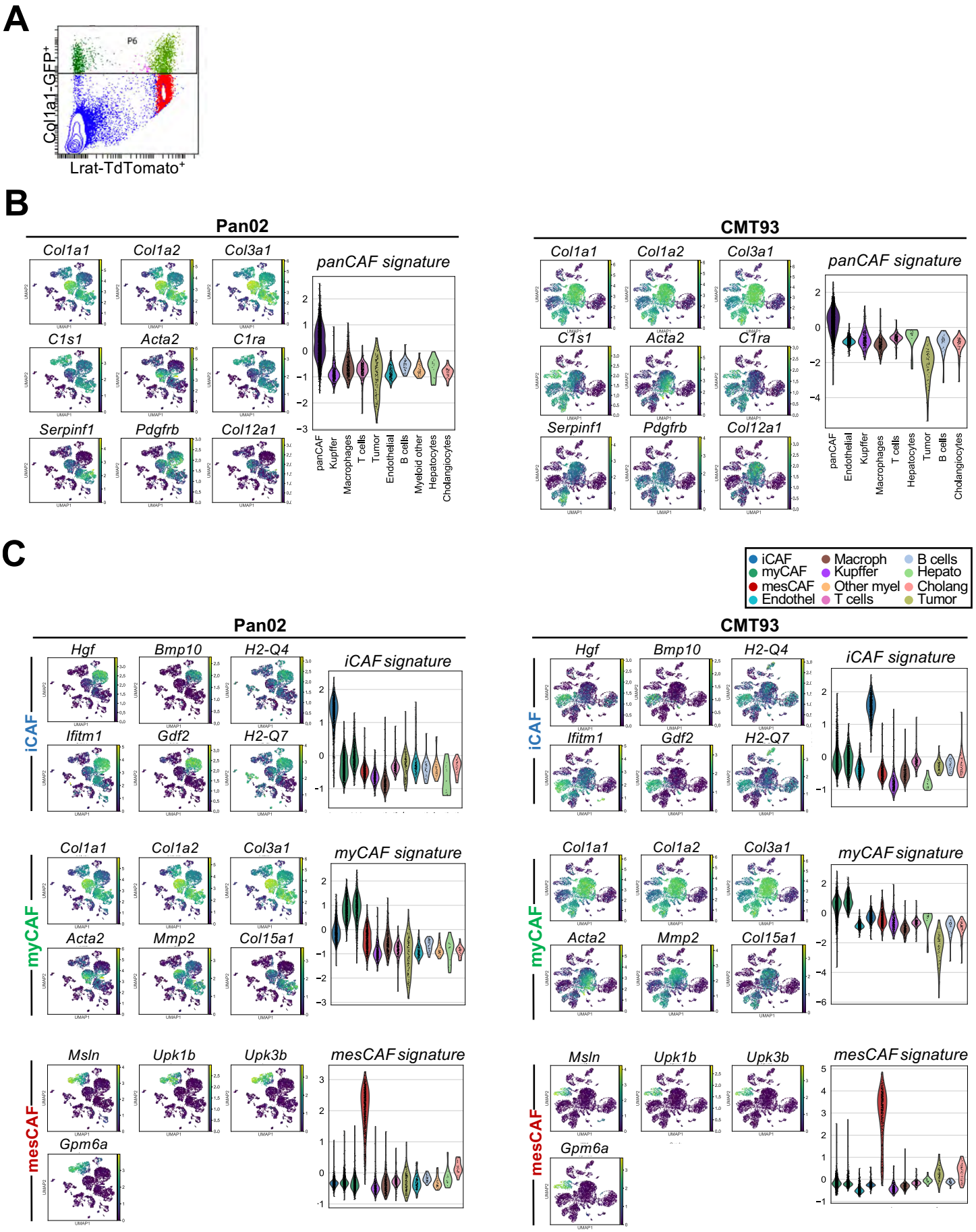

Fig. S2 | CAF characterization through single cell RNA-sequencing. A. Gating strategy used to sort CAF-enriched samples. 70% cells were taken from gate P6 (Col1a1-GFP positive) and 30% cells were from the live gate representing other populations. **B.** UMAPs showing genes used to determine panCAF signature in Pan02 and CMT93 liver metastasis model. **C.** iCAF, myCAF and mesCAF sgnatures and corresponding violin plots displaying all clusters with scores for iCAF, myCAF and mesCAF for Pan02 and CMT93 liver metastasis.

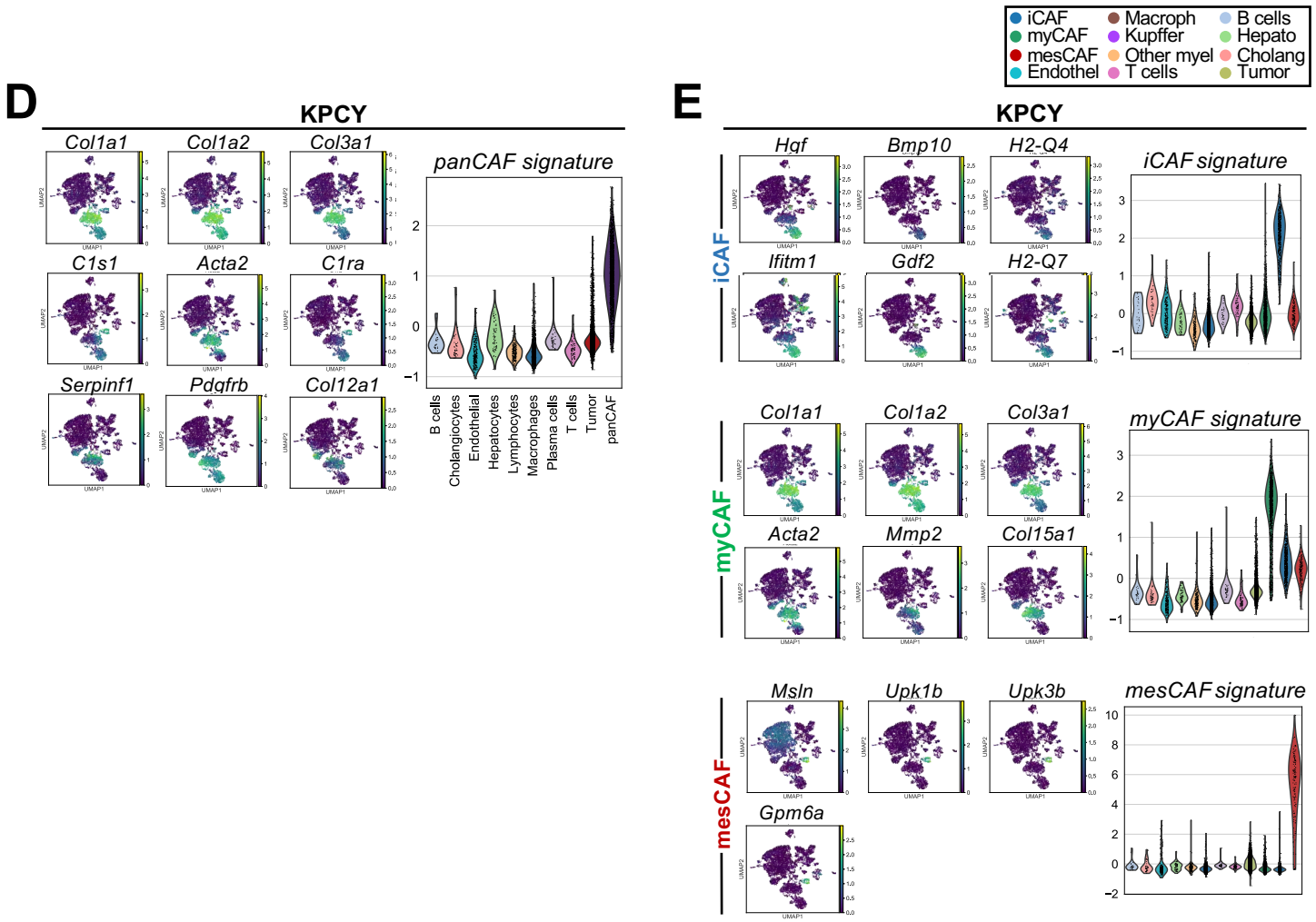

Fig. S2 | CAF characterization through single cell RNA-sequencing (continued). D. UMAPs showing genes used to determine panCAF signature in KPCY liver metastasis model. **E.** iCAF, myCAF and mesCAF sgnatures and corresponding violin plots displaying all clusters with scores for iCAF, myCAF and mesCAF for KPCY liver metastasis.

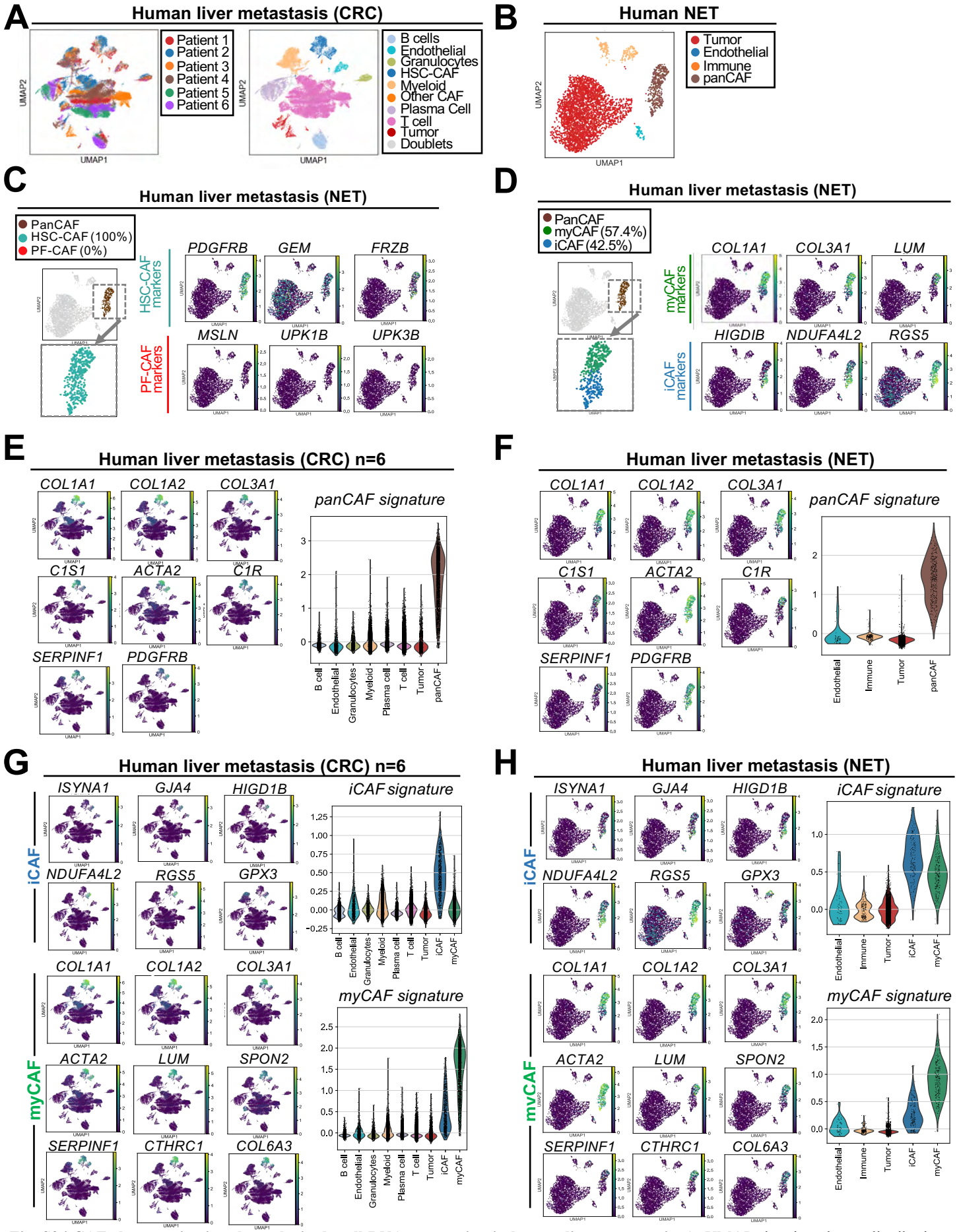

Fig. S3 | CAF characterization through single cell RNA-sequencing in human liver metastasis. A. UMAP showing cluster distribution of samples from 6 CRC liver metastasis patients **B.** UMAP displaying all cell populations acquired in 1 human small intestinal neuroendocrine tumor (NET) liver metastasis sample. **C.** UMAPs of scRNA-seq of NET metastasis, displaying HSC and PF as a percentage of panCAF; human HSC markers *PDGFRB, GEM*, *HAND2*, *LUM* and human PF markers *MSLN* and *UPK1B*. **D.** UMAPs showing percentages and markers of myCAF and iCAF subpopulations for human NET liver metastasis. **E-F.** UMAPs showing genes used to determine panCAF signature and violin plots showing the clusters with panCAF scores for human CRC (E, n=6) and NET (Fn=1) liver metastasis **G-H.** UMAPs showing genes used to determine iCAF, myCAF and mesCAF sgnatures and corresponding violin plots displaying all clusters with scores for iCAF, myCAF and mesCAF for human CRC (G, n=6) and NET liver metastasis (H, n=1).

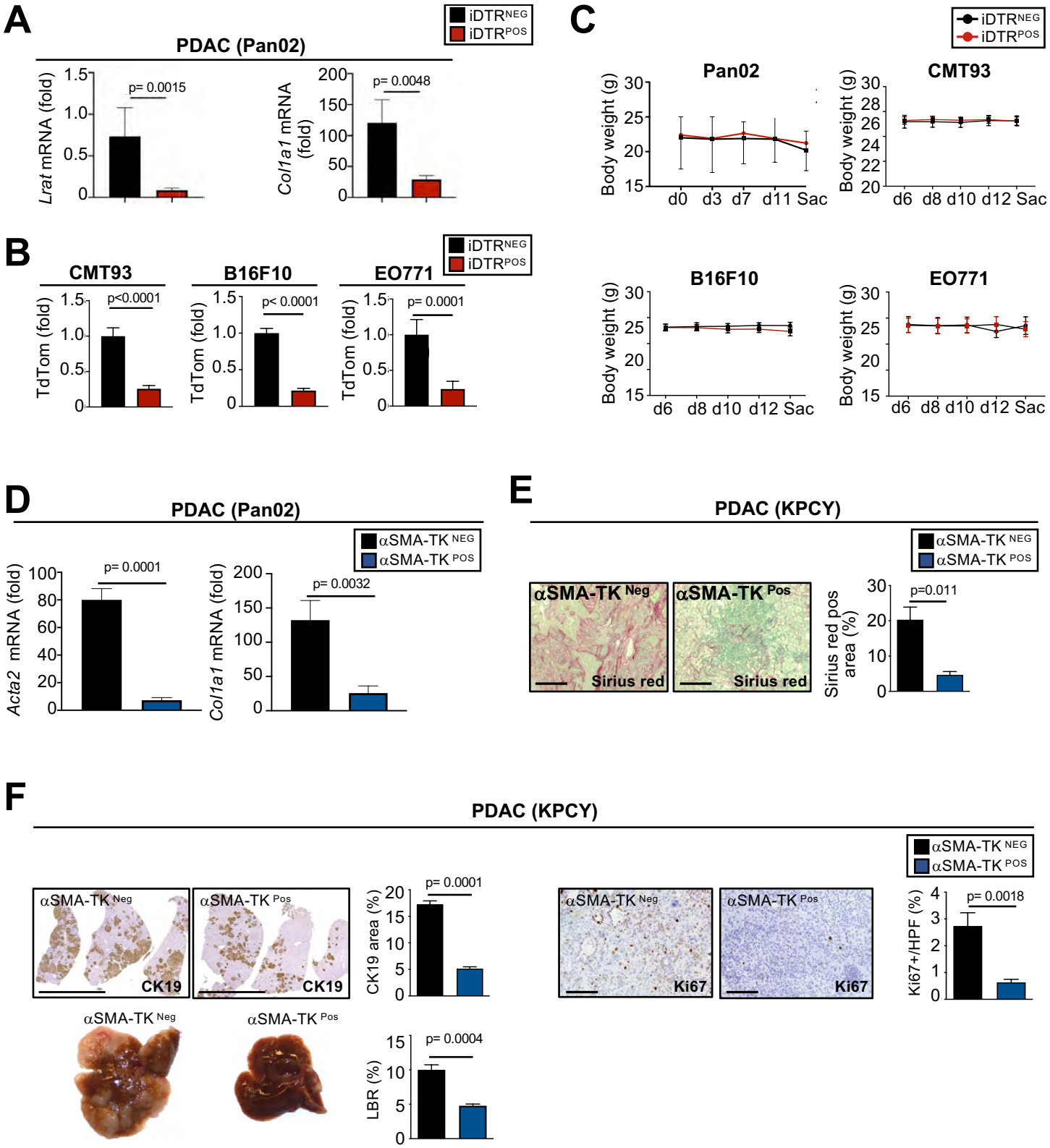

Fig. S4 | CAF promote desmoplastic tumor growth. HSC-CAF depletion via DT injection (0.5 ng/g) in LratCre+ TdTom+,iDTR+ or LratCre+ TdTom+ iDTR- littermates. **A.** mRNA levels of *Lrat* and *Col1a1* are reduced within tumor tissue in LratCre+ TdTom+,iDTR+ compared to LratCre+ TdTom+ iDTR- littermates. mRNA levels are shown as fold induction in comparison to normal liver tissue. **B-C.** DT injection reduces TdTom expression (B) but did not reduce body weight (C). **D.** mRNA levels of *Acta2* and *Col1a1* are reduced within tumor tissue in αSMA-TK positive mice compared to αSMA-TK negative littermates in the Pan02 metastasis model (n=6-10 mice/group). mRNA levels are shown as fold induction in comparison to normal liver tissue. **E-F.** αSMA-TK positive mice and αSMA-TK negative littermates were injected intrasplenically with KPCY cells. Representative Sirius red images and quantification (E, n=9-13 mice/group). Scale bars, 100 µm. Representative macroscopic and CK19 IHC images of liver, liver body weight ratio (LBR), tumor area quantifications and Ki67 quantifications (n=7 mice/group). Scale bars, 1cm (CK19) and 100 µm (Ki67). Statistics were done by two-tailed unpaired T-test or Mann Whitney-U. Data are displayed as mean ± SEM

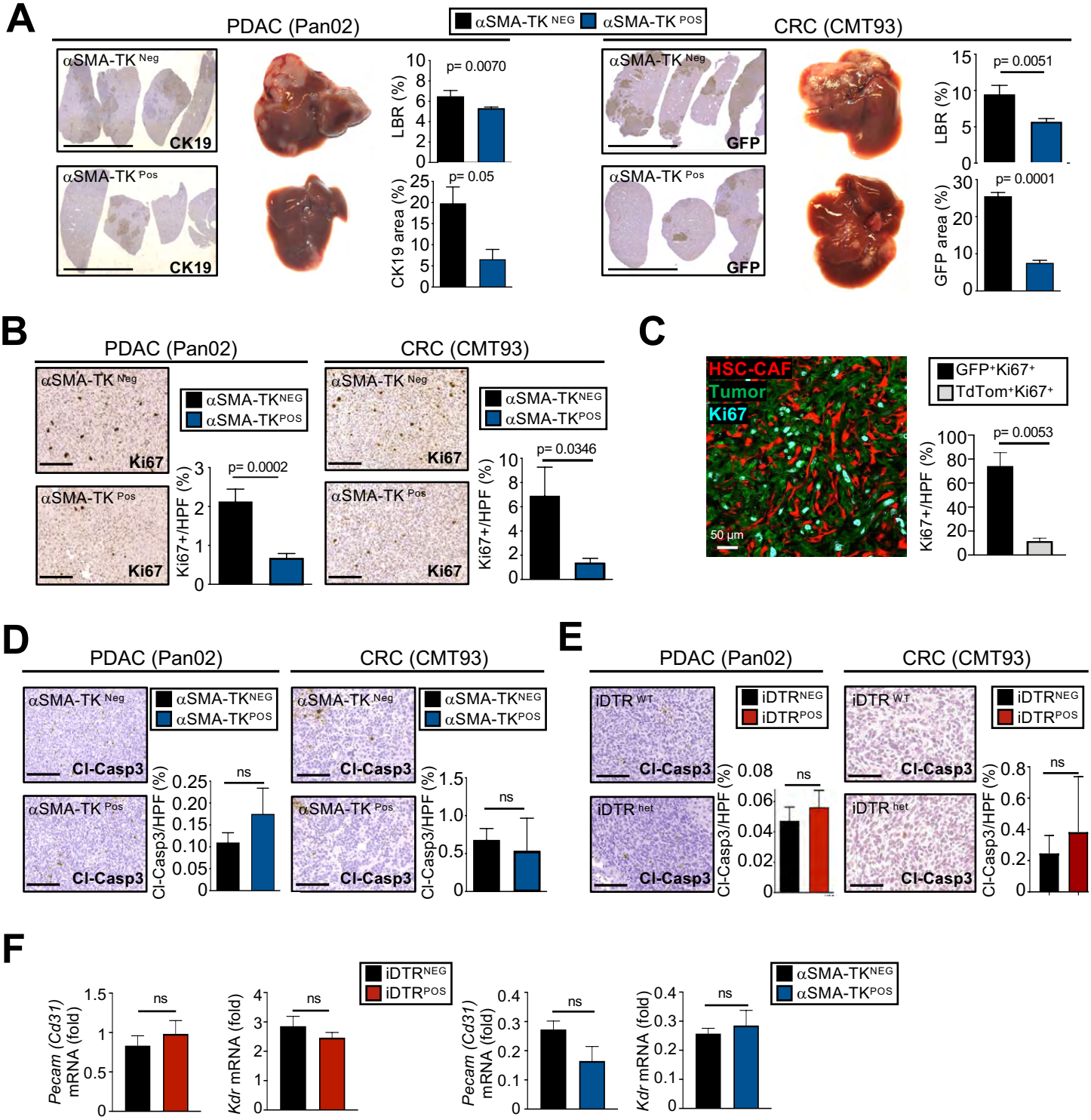

Fig. S5 | CAF promote tumor cell proliferation. A-B. Effect of αSMA-TK-mediated CAF depletion in αSMA-TK positive mice and αSMA-TK negative littermates (n=7-8 mice per group) on metastatic growth of Pan02 and CMT93 metastasis. Ganciclovir injections were administered daily from day 10 to day 13. Representative macroscopic and IHC images of liver, liver body weight ratio (LBR) and tumor area quantifications of αSMA-TK positive mice and αSMA-TK negative littermates (B), scale bars, 1 cm. Representative IHC images and quantification of Ki67+ cells (B); scale bars, 100 µm. **C.** Representative IF images and quantification of Ki67+ GFP+ cells compared to Ki67+TdTom+HSC cells in the Pan02 model in LratCre+ TdTom+ mice; scale bars, 50 µm. **D-E.** Representative IHC images and quantification of cleaved caspase 3+ cells in Pan02 and CMT93 models in αSMA-TK positive mice and αSMA-TK negative littermates as described in A-B; scale bars, 100 µm. **F.** mRNA levels of *Pecam* and *Kdr* in αSMA-TK and Lrat-iDTR mice in the Pan02 model. mRNA levels are shown as fold induction in comparison to normal liver tissue (n=6-10 per group). Statistics were done by two-tailed unpaired T-test or Mann Whitney-U. Data are displayed as mean ± SEM), ns stands for p value not significant.

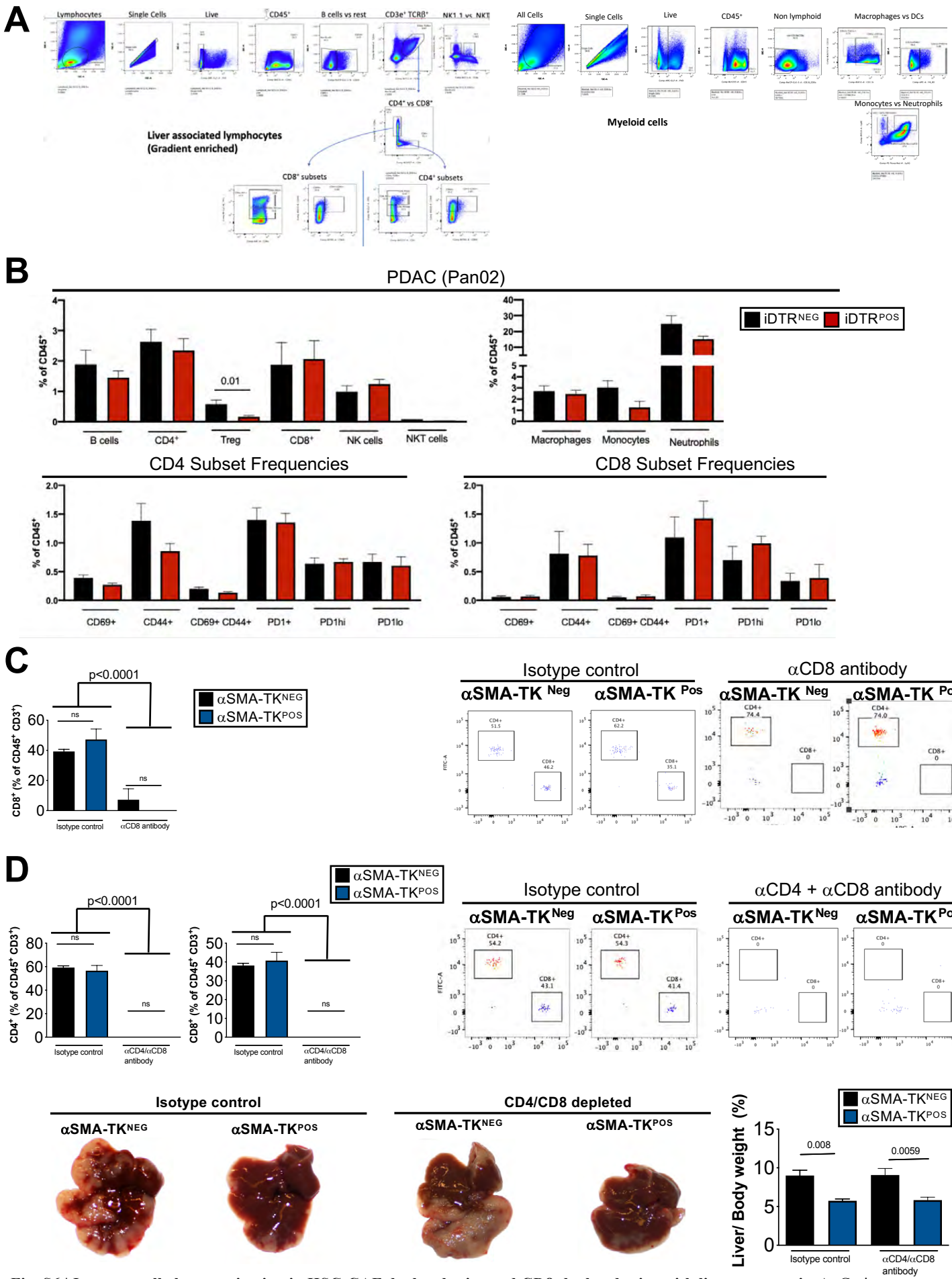

Fig. S6 | Immune cell characterization in HSC-CAF depleted mice and CD8-depleted mice with liver metastasis. A. Gating strategy of immune cells isolated from tumors from HSC-CAF depletion via DT injection (0.5 ng/g) at day 7 and day 10 in LratCre+ TdTom+,iDTR+ or LratCre+ TdTom+ iDTR- littermates. **B.** Immune cell population proportions as percent of CD45+ cells, **C.** Depletion efficiency of CD8 antibodies analyzed in blood samples collected from animals treated with antibody versus isotype control. **D.** CD4 and CD8 T-cell depletion or isotype injection in αSMA-TK mice injected with ganciclovir (i.p. 10 mg/kg) to deplete CAF simultaneously. Pan02 liver metastasis in αSMA-TK mice with representative macroscopic images of liver and liver body weight ratio (LBR) (n=5mice/group).

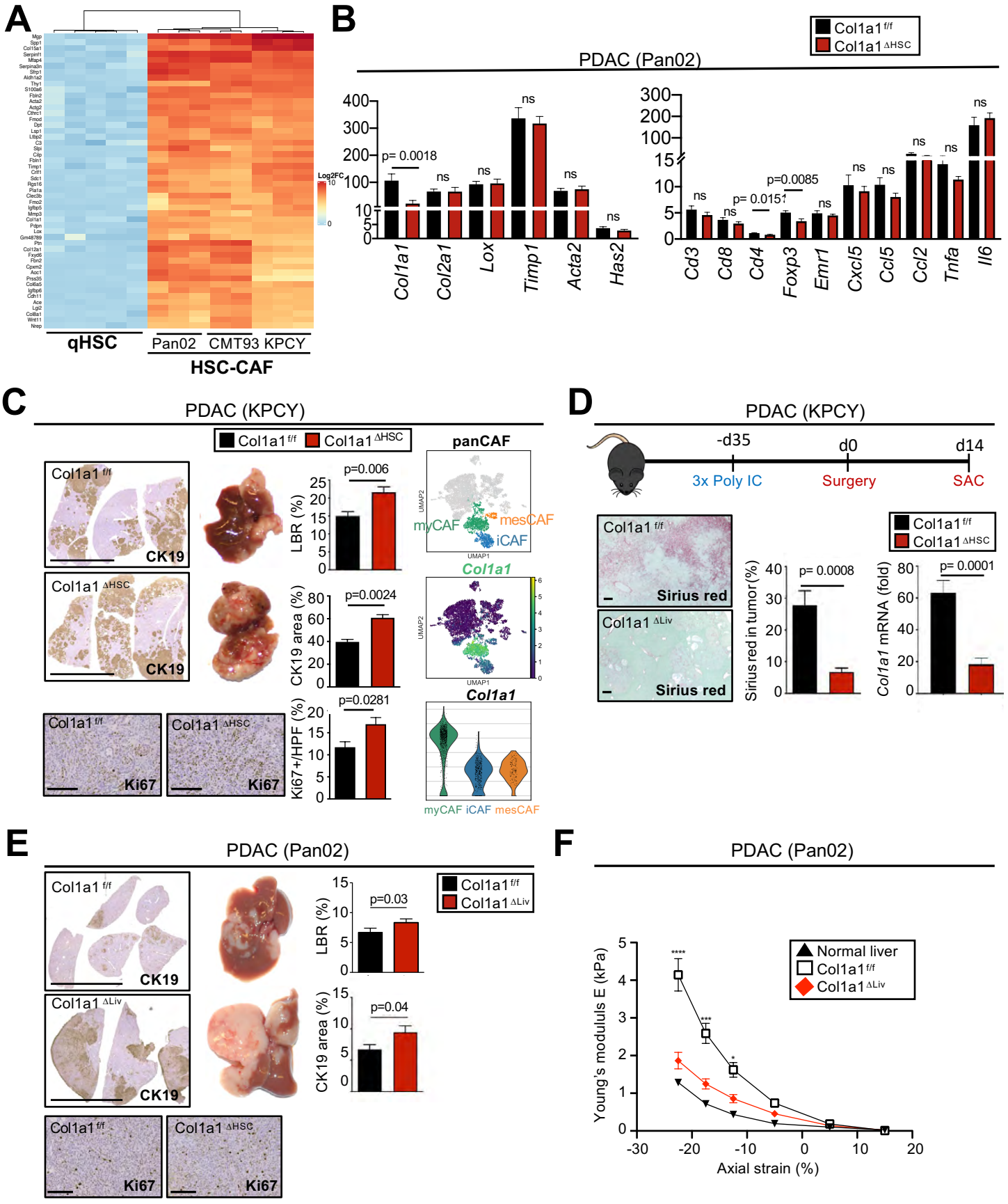

Fig. S7 | Col1a1 is strongly upregulated in CAF and its deletion promotes metastatic tumor growth while decreasing stiffness. A. Bulk RNA sequencing of purified quiescent HSC vs HSC-CAF shows top differentially expressed genes in HSC-CAF from Pan02, CMT93 and KPCY as ECM-associated. Top differentially expressed genes organized by log2fold change. **B.** mRNA levels of fibrosis-associated and immune cell-associated genes in Col1a1$^{f/f}$ vs Col1a1 $^{\Delta HSC}$ mice in the Pan02 model. mRNA levels are shown as fold induction in comparison to normal liver tissue. **C.** UMAPs and gene signatures of myCAF and *Col1a1* in KPCY (n=1). Representative macroscopic and IHC images of liver, liver body weight ratio (LBR), tumor area quantifications Ki67 quantifications (n=7 mice/group) injected with KPCY cells in Col1a1$^{f/f}$ vs Col1a1 $^{\Delta HSC}$ mice. Scale bars, 1cm (CK19) and 100µm (Ki67). **D.** Sirius red (n= 10-12 mice/group) of Mx1Cre-induced Col1a1 deletion. Scale bars, 100 µm. **E.** Representative macroscopic and IHC images of liver, liver body weight ratio (LBR), tumor area quantifications Ki67 quantifications (n=10-12 mice/group) injected with Pan02 cells in Mx1Cre^{pos} x Col1a1$^{fl/fl}$ (Col1a1$^{\Delta Liv}$) vs Col1a1$^{fl/fl}$ littermates. Scale bars, 1cm (CK19) and 100 µm (Ki67). **F.** Rheometry measurements in Mx1Cre^{pos} x Col1a1$^{fl/fl}$ (Col1a1$^{\Delta Liv}$) mice injected with Pan02 cells showing reduced stiffness in comparison to Col1a1$^{fl/fl}$ littermates. Statistics were done by two-tailed unpaired T-test or Mann Whitney-U. Data are displayed as mean ± SEM

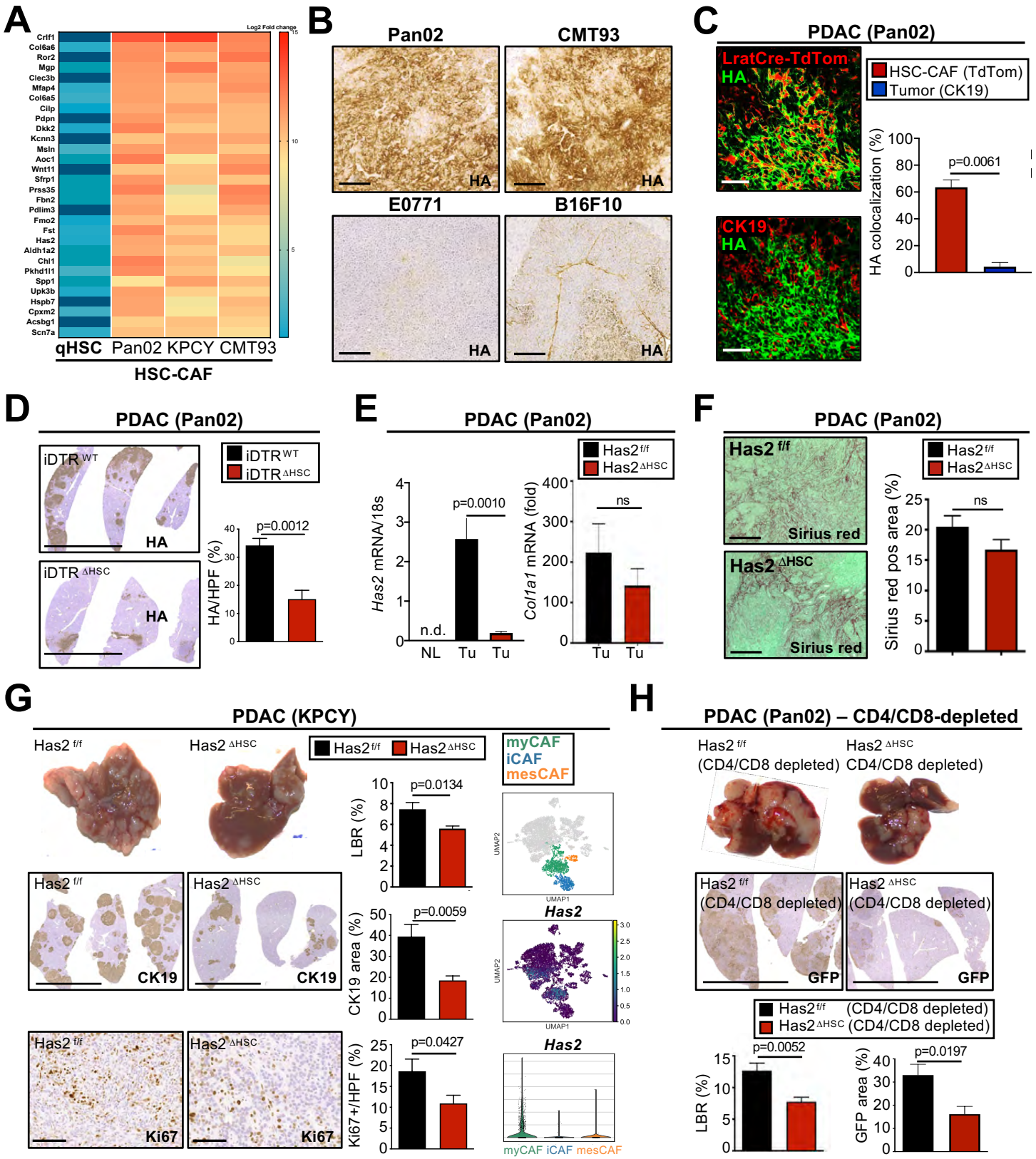

Fig. S8 | Hyaluronan promotes tumor cell growth. (A) Bulk RNAseq data comparing top 30 differentially expressed genes between qHSC (from normal liver) and CAF derived from Pan02 (n=3), KPCY (n=3) and CMT93 (n=2) models. Genes organized by pAdj value relative to quiescent sample. **(B)** HA staining in desmoplastic Pan02 and CMT93 as well as non-desmoplastic EO771 and B16F10 liver metastasis. Scale bars, 100 µm **(C)** The majority of HA colocalizes with LratCre x TdTom-positive HSC and not to CK19-positive tumor cells**.** Scale bar, 50µm **(D)** HA staining in LratCre^{pos} TdTom^{pos} iDTR^{pos} mice or LratCre^{pos} TdTom^{pos} iDTR^{neg} littermates, treated with 3x injections of DT (0.5 ng/g) reveals significantly reduced HA in HSC-CAF-depleted mice. Scale bar, 1cm **(E)** mRNA levels of Has2 are significantly decreasedwithin tumor tissue in Has2 $^{\Delta HSC}$ mice compared to Has2 $^{f/f}$ mice injected intra-splenically with Pan02 cells, and not detected ("n.d.") in normal liver. *Col1a1* mRNA levels are shown as fold induction in comparison to normal liver tissue and not altered by Has2 deletion. Tu= Tumor, NL= Normal liver **(F)** Sirius red staining reveals no differences in fibrosis between Has2$^{f/f}$ vs Has2 $^{\Delta HSC}$ mice. Scale bars, 100 µm **(G)** UMAPs and gene signatures of myCAF and *Has2* in KPCY (n=1). Representative macroscopic and IHC images of liver, the liver body weight ratio (LBR), tumor area and Ki67 quantifications (n=7-8 per group each) in Has2$^{f/f}$ vs Has2 $^{\Delta HSC}$ mice in the KPCY liver metastasis model. Scale bars, 1 cm (CK19) and 100 µm (Ki67). **(H)** To determine if CD4 and CD8 T cells were needed for tumor modulatory effects of HA, we investigated tumor development in the Pan02 liver metastasis model in Has2$^{f/f}$ vs Has2 $^{\Delta HSC}$ mice that were depleted of CD4+ and CD8+ T cell by antibody injections day 6 and day 11. Shown are macroscopic and IHC images of liver, liver body weight ratio (LBR) and tumor area quantifications. Scale bars, 1 cm. Statistics were done by two-tailed unpaired T-test or Mann Whitney-U. Data are displayed as mean ± SEM, ns stands for p value not significant.

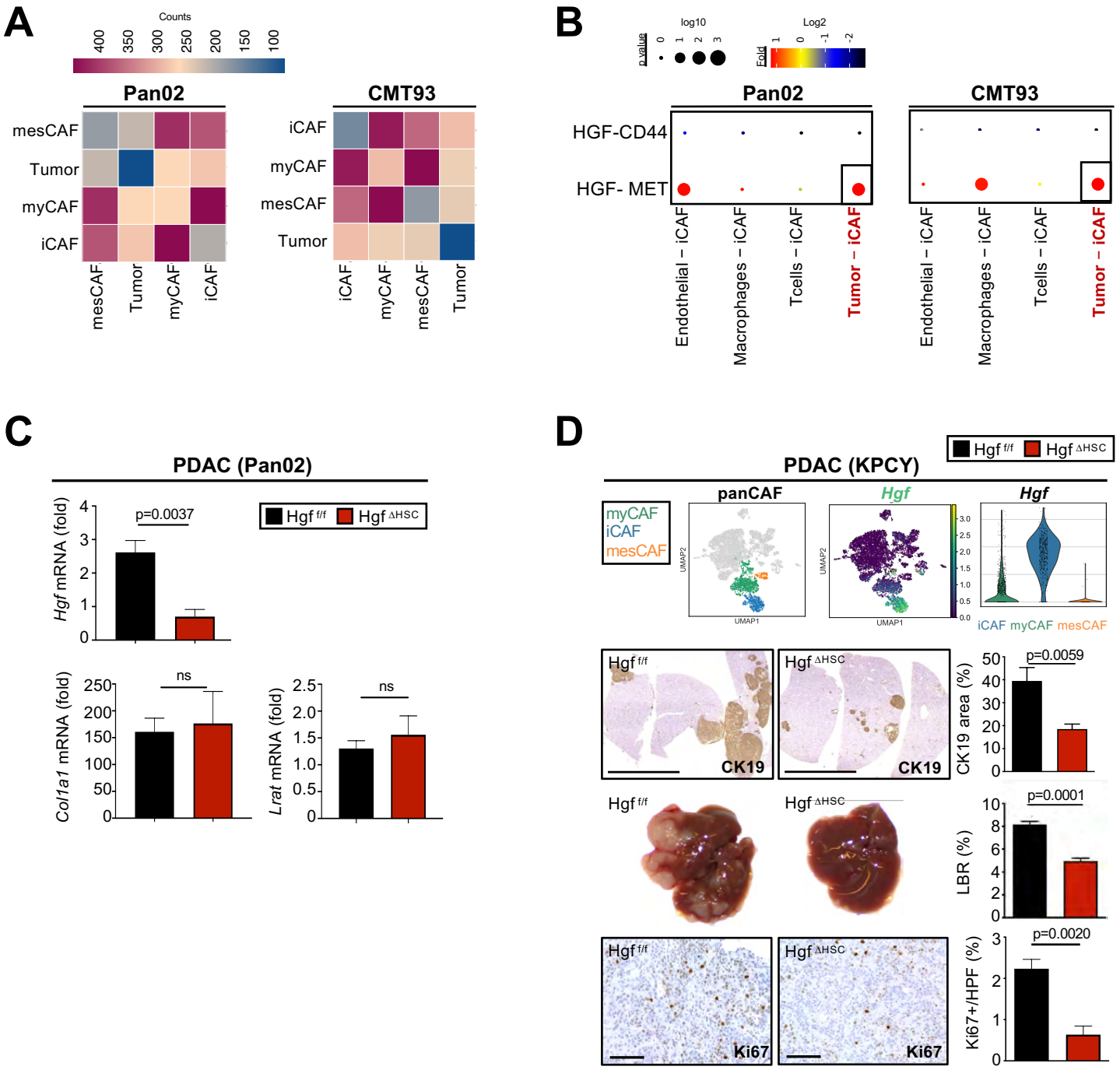

Fig. S9 | CAF expressed HGF links to tumor expressed MET and promotes tumor growth. A. CellphoneDB analysis showing ligand–receptor interactions between tumor cells with CAF subpopulations- iCAF, myCAF and mesCAF. **B.** CellphoneDB analysis showing all Hgf-receptor interactions for iCAF against all populations. **C.** mRNA levels of *Lrat* and *Col1a1* are unchanged within tumor tissue in Hgf $^{\Delta HSC}$ mice compared to Hgf $^{f/f}$ mice injected with Pan02 cells. mRNA levels are shown as fold induction in comparison to normal liver tissue. **D.** UMAPs and gene signatures of iCAF and *Hgf* in KPCY (n=1). Representative macroscopic and CK19 and Ki67 IHC images of liver, liver body weight ratio (LBR), tumor area and Ki67 quantifications (n=4 per group each) in the KPCY model of liver metastasis. Statistics were done by two-tailed unpaired T-test or Mann Whitney-U. Data are displayed as mean ± SEM. Scale bars 1 cm (CK19) and 100 µm (Ki67).

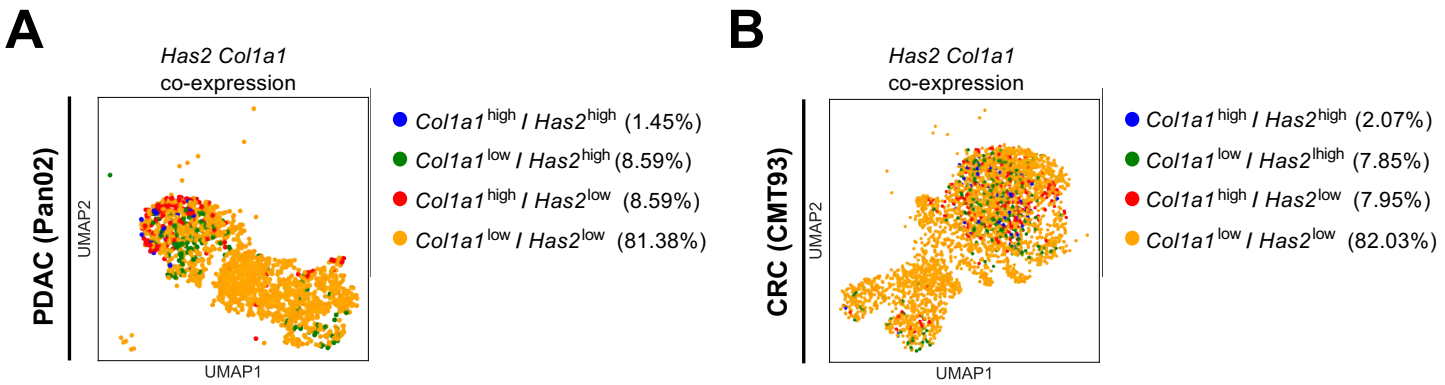

Fig. S10 | ScRNA-seq analysis of Col1a1 and Has2 co-expression in myCAF. A-B. UMAPs showing co-expression of *Has2* and *Col1a1* within myCAF populations in Pan02 (A) and CMT93 (B) metastasis models. Top 10% of each population is considered 'High'.

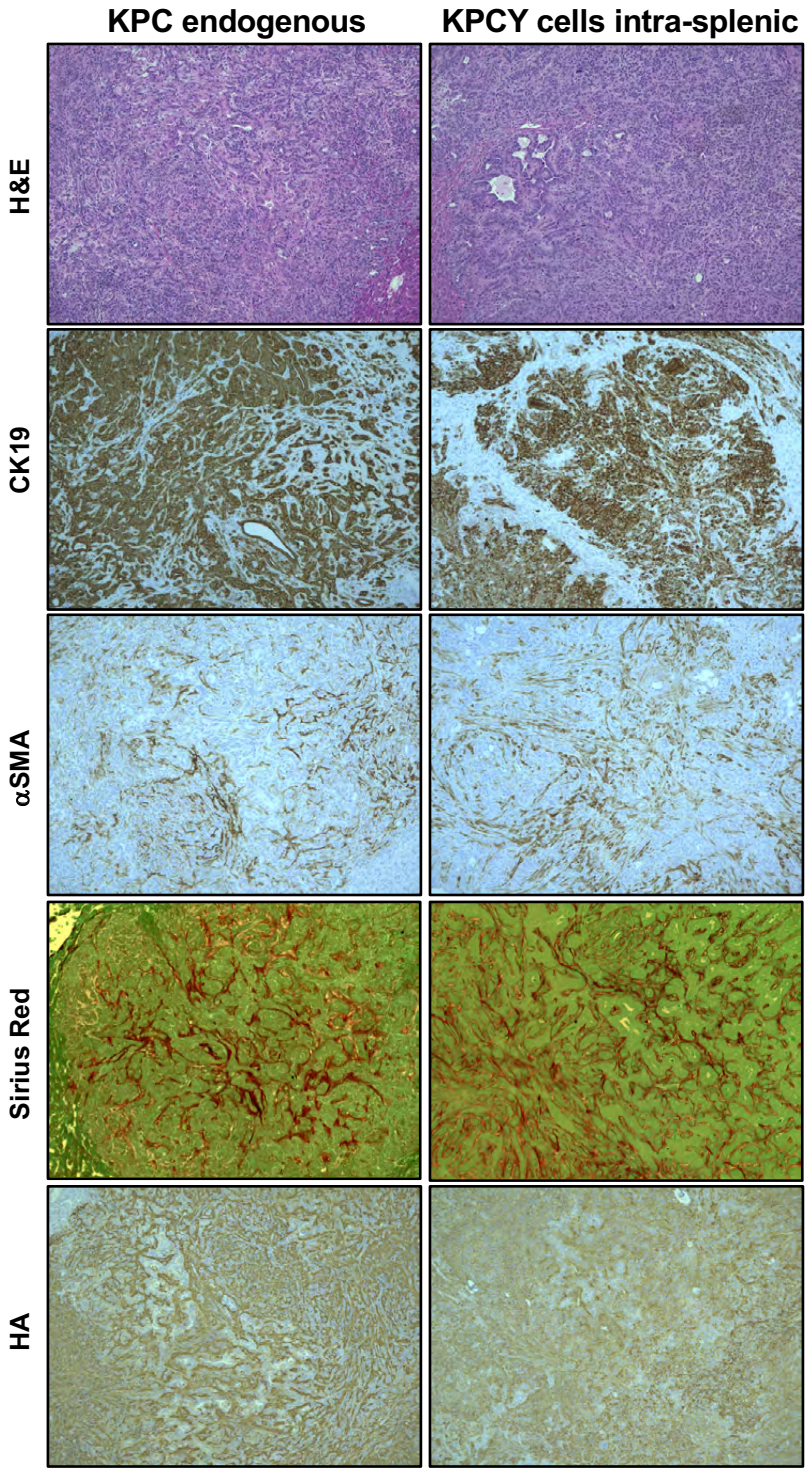

Fig. S11 | Comparison of endogenous KPC model with intra-splenic injected KPCY cells. Histological comparison of liver metastasis in endogenous KPC model with intra-splenic injection of KPCY cells in the liver. Scale bars, 100μm

Table S1. Cell marker genes for cell population identification and CAF subpopulations markers.

Mouse										
PanCAF	Col1a1	Col1a2	Col3a1	C1s1	Acta2	C1ra	Serpinf1	Pdgfrb	Col12a1	
HSC-CAF	Lrat	Des	Colec11	Rgs5	Cygb	Ednra	Frzb	Lum	Ndufa412	Sept4
PF-CAF	Msln	Upk1b	Upk3b	Gpm6a						
Tumor	Krt19	Epcam								
Endothelial	Kdr	vWf	Pecam1							
Hepatocytes	Alb	Ttr								
Myeloid	Adgre1	Cd68	Cd52	Itgam						
Lymphoid	Prprcap	Cd3e	Cd2	Cd19						
Cholangiocytes	Sctr	Hnf1b	Krt19	Epcam						

MOUSE myCAF	Atxn10	Col12a1	Ctla2a	Fbln1	H1f0	Ltbp2	Ndufa4l2	Pla1a	Rnf149	Slc7a2	Tnc
	Avpi1	Col15a1	Ctxn1	Fbln2	Heyl	Lxn	Nkd2	Pla2g16	Rnf19b	Slc7a5	Tnfaip2
	B4galnt1	Col1a1	Cx3cl1	Fbn2	Hs6st2	Maged2	Nrep	Plat	Runx1	Smco4	Tppp3
	Bhlhe41	Col1a2	Cxcl14	Fgfr1	Htra1	Map1b	Nrp2	Plaur	S100a16	Smim3	Tsc22d3
Ace	Bmp1	Col3a1	Cyp51	Fkbp11	Igfbp5	Mapkapk3	Nuak1	Plod2	S100a4	Sox4	Ttll5
Acot7	Bpgm	Col4a5	Dap	Frem1	Igsf3	Mdfi	Ociad2	Plp2	Sac3d1	Sparcl1	Tubb2a
Acta2	Capg	Col5a2	Dbp	Fst	Impdh1	Mdk	Olfml2b	Plpp5	Scpep1	Specc1	Tubb3
Actg2	Cd59a	Col5a3	Ddah1	Fstl1	Inhba	Medag	P4ha2	Pmepa1	Sdc1	Spp1	Tyms
Adam19	Cd9	Col6a2	Dpysl3	Fstl3	Itm2a	Meox1	Pafah1b3	Podxl2	Serf1	Srpx	Uck2
Adcy7	Cd93	Col7a1	Ebf1	Fxyd5	Kctd11	Mfap2	Palld	Prrx1	Serpine2	Stc2	Vcan
Ahnak2	Cda	Col8a1	Egln3	Fxyd6	Kdelr3	Mfap4	Pcbp4	Prss35	Serpinf1	Stk17b	Vegfa
Ak1	Cdh11	Colec12	Emp1	Fzd1	Kif26b	Mgll	Pdgfrl	Ptgfrn	Sesn3	Sulf1	Vmp1
Akr1b8	Cdkn2a	Comtd1	Eno1	Gapdh	Kremen1	Mgp	Pdlim3	Ptk7	Sfrp1	Tfpi2	Wisp1
Aldh1a2	Cdkn2b	Copz2	Enpp1	Gas7	Lama4	Mical2	Pdzrn3	Ptn	Sh3bgrl3	Tgfb3	Wnt11
Ank	Cercam	Cotl1	Etv4	Gm15867	Lef1	Minos1	Pgam1	Ptprb	Sh3pxd2b	Thy1	Zswim7
Ankrd37	Ch25h	Cox4i2	Evl	Gng11	Lefty1	Mmp14	Pgf	Rab7b	Shisa4	Thyn1	
Anpep	Chst11	Cpxm2	Fam198b	Gpbar1	Lgals1	Mmp2	Pgk1	Rap2b	Siva1	Timp1	
Aoc1	Chst2	Crlf1	Fam20a	Gpc1	Lgi2	Mtch1	Piezo2	Rapgef4	Slc16a3	Tm4sf1	
Apol9a	Clec11a	Csrp2	Fam20c	Gpm6b	Lhfpl2	Nbl1	Pik3ip1	Rgs16	Slc27a1	Tmem2	
Aprt	Clmp	Cthrc1	Fam69b	Gpr153	Lsp1	Ncam1	Pkm	Rgs19	Slc39a14	Tmem45a	

MOUSE iCAF	Angptl6	C2	Cyp27a1	Ephb4	Gns	Ifnar2	Lrrc4c	Nrxn1	Rasgef1b	Slc35d1	Tmem51
	Ank3	C4b	Cyr61	Etnk1	Gpat2	Igf1r	Ltbp1	Nrxn2	Rasgrp2	Slc40a1	Tmem56
	Ankrd55	C6	Cysltr1	Ets1	Gpc4	Iigp1	Ly6e	Ntf3	Rasl11a	Slc4a8	Tmem9b
Aard	Ano1	Cachd1	D1Ertd622e	Ets2	Grap	Il10rb	Macf1	Ntm	Rbfox3	Slc9a3r2	Tmtc2
Abcc9	Apoc1	Cadm3	430019H16R	Eva1b	Gstm1	Il11ra1	Man1a	Ntn1	Rbm46	Slco2b1	Tnfrsf11b
Abi3bp	Apoe	Calcrl	Daam2	Fam171b	Gstt1	Il6st	Man2a1	P2ry14	Rbpms	Slco3a1	Tnfrsf1b
Ablim2	Apold1	Camk1d	Dapk1	Fam26f	H2-D1	Itga1	Map4k3	P3h2	Rcsd1	Slmap	Tnfrsf21
Acap1	Arap2	Ccbe1	Dapk2	Fam49a	H2-K1	Itga2b	Marcks	Pam	Reln	Smad6	Tns1
Acer2	Arhgap24	Ccdc3	Dcdc2a	Fam84a	H2-Q4	Itga9	Matn2	Papss2	Rem1	Smagp	Tns2
Acsl5	Arhgap42	Ccdc68	Dcn	Fbln5	H2-Q6	Itgb3	Mbd2	Parp14	Rgl1	Smpdl3a	Tnxb
Actn4	Arhgef6	Cd302	Ddr2	Fcna	H2-Q7	Itih3	Mertk	Pde1a	Rgs2	Sntg1	Trib2
Acvr2a	Arid5b	Cdc42ep4	Dennd2a	Fermt2	H6pd	Itih4	Metrn	Pde3a	Rgs4	Socs3	Trim30a
Adam23	Arrb1	Cdh2	Des	Fgfr2	Hand2	Itm2c	Mndal	Pdgfra	Rgs5	Sod3	Trp53i11
Adamts1	Art3	Cdk18	Dmd	Fhl1	Hdac7	Itpripl1	Ms4a4d	Pear1	Rhobtb1	Sorbs1	Tshz2
Adamts10	Arvcf	Cebpb	Dock8	Filip1l	Hes1	Jade2	Mt1	Phactr2	Rnaset2b	Sox5	Tspan7
Adamts13	Astn2	Chst15	Dse	Fos	Hexim1	Jun	Mt2	Pim1	Rock2	Sprn	Vipr1
Adamts5	Atp1a4	Cited2	Dusp1	Fosb	Hgf	Junb	Mtus1	Pim3	Rspo3	Ssfa2	Vstm4
Adamtsl2	AW112010	Cks2	Dusp10	Foxf1	Hhip	Jup	Mustn1	Pkia	Rtn1	St3gal4	Wipf1
Adap2	B2m	Clca3a1	Ece1	Frzb	Hlx	Kcnip3	Myc	Pla2r1	Rtn4rl1	Steap4	Xdh
Adap2os	Bambi	Clec14a	Ecm1	G0s2	Hmcn1	Kcnj8	Mylip	Plekha6	Rxra	Stim1	Zbtb16
Adgrl1	Bcl2l1	Clstn3	Ednra	Gab1	Hpse	Klf15	Mylk	Plscr4	Ryk	Susd2	Zbtb20
Adm	Bco1	Col14a1	Ednrb	Gabra3	Hs3st3a1	Klf9	Myo18a	Plvap	Scarb1	Syde1	Zfp36
Adora2a	Bcr	Colec10	Efemp1	Gdf10	Hs3st3b1	Ktn1	Myo1b	Plxnc1	Sdc4	Syt9	Zfp36l1
Adra2b	Birc2	Colec11	Egr1	Gdf2	Hsd11b1	Lama1	Ncoa7	Ppp1r14a	Selenbp1	Tbx20	Zfp703
Afap1l2	Birc3	Cp	Ehbp1	Gem	Icam1	Ldlrap1	Nfia	Prelp	Sema3d	Tcf21	
Agtr1a	Bmp10	Cped1	Ehd3	Ggt5	Id3	Lgals3bp	Nfkbia	Prex2	Sema4b	Tgfbi	
Agtrap	Bmp2	Cpne8	Eif4e3	Gja4	Ier2	Lhx2	Ngf	Prss23	Sema6d	Tgfbr3	
Alcam	Bmp5	Crip2	Emilin1	Gm10600	Ifi203	Lifr	Ngfr	Ptafr	Serpina3g	Tinagl1	
Aldh1a1	Bmyc	Csf1	Eng	Gm12216	Ifi27l2a	Lipa	Nkd1	Pth1r	Serping1	Tmem141	
Aldh1a3	Bok	Ctso	Enpp5	Gm12840	Ifih1	Lrat	Notch1	Ptprk	Sft2d2	Tmem176a	
Aldh2	Btg2	Cxcl12	Epas1	Gm13889	Ifit3	Lrp4	Npr3	Ramp1	Sgk1	Tmem178	
Alpl	C1ra	Cygb	Epb41l2	Gm14964	Ifitm1	Lrp5	Nr1h4	Ramp2	Shisa3	Tmem204	
Angptl2	C1s1	Cyp20a1	Epha2	Gm37800	Ifitm2	Lrrc32	Nr1h5	Raph1	Slc29a1	Tmem47	

MOUSE mesCAF							
Adgrd1	Cd2ap	Flrt2	Igfbp6	Mmd	Rbbp8	Slc9a3r1	Tmem98

Angptl7	Celf2	Fth1	Il18	Msln	Rspo1	Slpi	Tnfaip3
Anxa3	Cpe	Gas6	Krt18	Ndrg1	S100a1	Smpd3	Tnfrsf12a
Atp1b1	Cxadr	Gm20186	Krt7	Ndufa4	Saa3	Snrpg	Trf
Bicd1	Dab2	Gm8186	Krt8	Nkain4	Sbsn	Spint2	Ucp2
C3	Ddr1	Gpc3	Ldhb	Pdgfc	Serpinb6b	Stmn1	Upk1b
Cd151	Ezr	Gpm6a	Lgals3	Pdpn	Shb	Tcea3	Upk3b
Cd200	Fbxo33	Hspb1	Lrrn4	Rab11a	Slc39a8	Tmem151a	Wt1

HUMAN									
PanCAF	COL1A1	COL1A2	COL3A1	C1S	ACTA2	C1R	SERPINF1	PDGFRB	
HSC	RGS5	LUM	COLEC11	DCN	PDGFRB	GEM	TAGLN	CYGB	SERPINF1
	EDNRA	EMILIN1	FOXS1	FRZB	HEYL	NDUFA4L2	NOTCH3	SEPT4	COL14A1
PF	MSLN	UPK1B	KRT19	SLPI					
Tumor	KRT19	EPCAM							
Endothelial	KDR	VWF	ERG						
Hepatocyte-like	ALB	TTR							
T cell	CD3E	CD3D	CD3G	CD8A					
B cell	CD79A	CD79B							
Plasma cell	JSRP1	FCRL5							
Mast cell	CPA3	TPSAB1	KIT						
DC-like cell	ITGAX								
Monocytes	CD68	CD74	CD14	CSF1R					
Macrophaged	VSIG4	CD68	FCGR2A	CD163					

HUMAN myCAF										
APOD	CCL11	COL1A1	COL1A2	COL3A1	COL5A1	COL6A3	CTGF	CTHRC1	CYP1B1	FN1
INHBA	ISLR	LUM	MMP14	POSTN	PTGDS	SERPINF1	SFRP2	SPON2	VCAN	

HUMAN iCAF									
ADAMTS4	AGT	APOE	ARHGDIB	CCL19	CCL21	COLEC11	CPE	GEM	GJA4
GPX3	HIGD1B	IL6	ISYNA1	LHFP	MAP1B	MT1A	NDUFA4L2	PDK4	RGS5

HUMAN mesCAF									
ANXA1	ANXA2	BDKRB1	C19orf33	C3	CALB2	CCDC80	CFB	CRABP2	
CXCL1	CXCL6	EFEMP1	EGFL6	EMP3	EZR	HMOX1	HP	HSPA6	
IFI27	IGFBP6	ITLN1	KRT18	KRT19	KRT8	LINC01133	LOX	MT1E	
MT1G	MT1X	MXRA5	PDPN	PLA2G2A	PRG4	PRSS23	PTGIS	RP11-572C15.6	
S100A10	S100A16	S100A6	SAA1	SAA2	SERPINE2	SH3BGRL3	SLC12A8	SLPI	TM4SF1

Table S2. Top HSC-CAF/tumor interactions in CRC and PDAC liver metastasis.

Combined Rank Pan02, KPCY and CMT93	Interacting ligand-receptor pair	Rank Pan02	Signficant means HSC-CAF/tumor interactions (Pan02)	Rank KPCY	Signficant means HSC-CAF/tumor interactions (KPCY)	Rank CMT93	Signficant means HSC-CAF/tumor interactions (CMT93)
1	COL3A1_DDR1	2	37.435	3	23.842	1	41.029
2	COL3A1_a2b1 complex	3	37.405	1	24.078	3	40.783
3	COL3A1_DDR2	1	37.484	4	23.626	2	40.818
4	COL3A1_a1b1 complex	4	37.391	2	23.861	4	40.757
5	**COL1A1_DDR1**	10	**17.063**	7	**20.402**	5	**26.889**
6	COL1A1_a2b1 complex	11	17.033	5	**20.637**	7	**26.643**
7	**COL1A1_DDR2**	9	**17.112**	8	**20.186**	6	**26.677**
8	COL1A1_a1b1 complex	12	17.019	6	**20.42**	8	**26.617**
9	COL1A2_DDR1	6	18.767	11	18.666	9	24.247
10	COL1A2_a2b1 complex	7	18.737	9	18.901	11	24.001
11	COL1A2_DDR2	5	18.816	12	18.45	10	24.036
12	COL1A2_a1b1 complex	8	18.724	10	18.684	12	23.975
13	FN1_a3b1 complex	14	3.617	13	11.382	14	3.842
14	COL14A1_a2b1 complex	13	6.102	21	3.722	13	4.727
15	FN1_a2b1 complex	17	3.418	14	11.231	16	3.626
16	FN1_a2Bb3 complex	15	3.508	16	10.776	17	3.569
17	FN1_a4b7 complex	18	3.381	15	10.786	15	3.677
18	COL5A2_DDR1	22	2.585	20	3.861	18	3.546
19	COL6A3_a2b1 complex	16	3.493	22	3.523	22	3.108
20	COL4A1_DDR1	20	2.826	18	6.358	24	2.669
21	COL5A2_a2b1 complex	23	2.555	19	4.097	20	3.3
22	COL4A1_a2b1 complex	21	2.796	17	6.593	26	2.423
23	LAMP1_FAM3C	19	3.33	29	2.094	19	3.487
24	COL5A1_DDR1	25	2.157	26	3.179	25	2.519
25	COL5A1_a2b1 complex	26	2.127	24	3.414	27	2.273
26	THBS1_a3b1 complex	30	1.803	30	1.969	21	3.231
27	COL6A2_a2b1 complex	24	2.493	33	1.636	31	1.837
28	**HGF_CD44**	29	**1.864**	28	**2.366**	34	**1.453**
29	COL4A2_a2b1 complex	36	1.499	25	3.311	33	1.548
30	COL4A2_DDR1	35	1.529	27	3.076	32	1.794
31	MMP2_aVb3 complex	27	1.958	45	0.915	23	2.888
32	TNFSF12_TNFRSF12A	33	1.612	34	1.578	28	2.243
33	COL15A1_a2b1 complex	40	0.971	23	3.51	40	0.985
34	LGALS9_CD44	37	1.194	32	1.738	37	1.333
35	IGF1_IGF1R	28	1.908	50	0.756	29	2.081
36	IGF1_a6b4 complex	31	1.775	42	1.051	35	1.399
37	LAMC1_a6b1 complex	38	1.01	31	1.75	42	0.955
38	VCAM1_a4b7 complex	34	1.598	51	0.729	30	1.907
39	RSPO3_LGR6	32	1.695	43	1.032	41	0.985
40	HAS1-HA-ligand_CD44	41	0.865	40	1.187	39	1.004
41	LAMC1_a2b1 complex	39	1.01	37	1.269	46	0.921
42	FGF2_CD44	44	0.735	36	1.281	44	0.928
43	**HAS2-HA-ligand_CD44**	47	**0.626**	35	**1.282**	45	**0.925**
44	TNC_aVb6 complex	50	0.435	44	1.012	38	1.012
45	MDK_SORL1	46	0.675	53	0.617	36	1.363
46	COL12A1_a2b1 complex	51	0.39	46	0.906	43	0.948
47	LGALS9_MET	45	0.713	48	0.815	48	0.729
48	COL8A1_a2b1 complex	52	0.368	41	1.165	49	0.706
49	PROS1_TYRO3	42	0.856	54	0.579	47	0.857
50	COL16A1_a2b1 complex	49	0.467	47	0.837	51	0.514
51	TGFB1_aVb6 complex	56	0.308	39	1.229	52	0.446
52	COL6A5_a2b1 complex	43	0.752	55	0.522	50	0.571
53	COL5A3_a2b1 complex	60	0.273	38	1.238	62	0.245
54	COL27A1_a2b1 complex	54	0.358	52	0.706	55	0.328
55	CSPG4_a3b1 complex	57	0.293	49	0.764	57	0.296
56	CADM3_EPB41L1	48	0.525	63	0.222	53	0.411
57	COL6A6_a2b1 complex	53	0.363	57	0.484	54	0.368
58	EPHB2_EFNB2	55	0.346	61	0.273	60	0.249
59	NOTCH1_DLL4	59	0.276	59	0.38	59	0.251
60	NOTCH1_JAG2	58	0.287	58	0.422	61	0.248
61	**HAS2-HA-ligand_HMMR**	62	**0.236**	62	**0.269**	56	**0.319**
62	NRG1_a6b4 complex	64	0.157	56	0.505	65	0.12
63	NOTCH3_JAG2	63	0.229	60	0.35	63	0.217
64	IL1 receptor inhibitor_IL1	65	0.11	65	0.175	58	0.285
65	EPHB6_EFNB2	61	0.267	64	0.211	64	0.187
66	NOTCH4_JAG2	66	0.025	66	0.122	66	0.058

Table S3. 43 novel CellPhoneDB ligand-receptor interactions.

Ligand-receptor	Ligand Name	Ligand ID	Receptor name	Receptor ID	PMID Reference
COL1A1 - DDR1	COL1A1	P02452	DDR1	Q08345	PMID: 32047176 ; PMID: 32244515 ; PMID: 28590245 ; PMID: 31004686
COL1A2 - DDR1	COL1A2	P08123	DDR1	Q08345	PMID: 32047176 ; PMID: 32244515 ; PMID: 28590245 ; PMID: 31004686
COL2A1 - DDR1	COL2A1	P02458	DDR1	Q08345	PMID: 33234027 ; PMID: 31004686
COL3A1 - DDR1	COL3A1	P02461	DDR1	Q08345	PMID: 28743124 ; PMID: 31004686 ; PMID: 21421911
COL5A1 - DDR1	COL5A1	P20908	DDR1	Q08345	PMID: 33234027 ; PMID: 31004686 ; PMID: 23861322
COL5A2 - DDR1	COL5A2	P05997	DDR1	Q08345	PMID: 23861322
COL5A3 - DDR1	COL5A3	P25940	DDR1	Q08345	PMID: 23861322
COL11A1 - DDR1	COL11A1	P12107	DDR1	Q08345	PMID: 31717573
COL11A2 - DDR1	COL11A2	P13942	DDR1	Q08345	PMID: 31717573
COL1A1 - DDR2	COL1A1	P02452	DDR2	Q16832	PMID: 31699892 ; PMID: 21421911
COL1A2 - DDR2	COL1A2	P08123	DDR2	Q16832	PMID: 31699892 ; PMID: 21421911
COL2A1 - DDR2	COL2A1	P02458	DDR2	Q16832	PMID: 31958497
COL3A1 - DDR2	COL3A1	P02461	DDR2	Q16832	PMID: 28743124 ; PMID: 21421911
COL5A1 - DDR2	COL5A1	P20908	DDR2	Q16832	PMID: 33234027 ; PMID: 23861322
COL5A2 - DDR2	COL5A2	P05997	DDR2	Q16832	PMID: 23861322
COL5A3 - DDR2	COL5A3	P25940	DDR2	Q16832	PMID: 23861322
COL11A1 - DDR2	COL11A1	P12107	DDR2	Q16832	PMID: 29769618
COL11A2 - DDR2	COL11A2	P13942	DDR2	Q16832	PMID: 31717573
COL4A1 - DDR1	COL4A1	P02462	DDR1	Q08345	PMID: 23861322
COL4A2 - DDR1	COL4A2	P08572	DDR1	Q08345	PMID: 23861322
COL4A3 - DDR1	COL4A3	Q01955	DDR1	Q08345	PMID: 23861322
COL4A4 - DDR1	COL4A4	P53420	DDR1	Q08345	PMID: 23861322
COL4A5 - DDR1	COL4A5	P29400	DDR1	Q08345	PMID: 23861322
COL4A6 - DDR1	COL4A6	Q14031	DDR1	Q08345	PMID: 23861322
COL10A1 - DDR2	COL10A1	Q03692	DDR2	Q16832	PMID: 33324550
HAS1-HA - CD44	HAS1-HA-ligand	Undefined	CD44	P16070	PMID: 24406795 ; PMID: 31276783 ; PMID: 18661346
HAS1-HA - HMMR	HAS1-HA-ligand	Undefined	HMMR	O75330	PMID: 31276783 ; PMID: 24668563
HAS1-HA - ICAM1	HAS1-HA-ligand	Undefined	ICAM1	P05362	PMID: 16449361 ; PMID: 8867647
HAS1-HA - TLR4	HAS1-HA-ligand	Undefined	TLR4	O00206	PMID: 21248167 ; PMID: 31484704
HAS1-HA - TLR2	HAS1-HA-ligand	Undefined	TLR2	O60603	PMID: 21248167 ; PMID: 28682809 ; PMID: 20534434
HAS1-HA - LYVE1	HAS1-HA-ligand	Undefined	LYVE1	Q9Y5Y7	PMID: 12554094 ; PMID: 19033446 ; PMID: 30054204
HAS2-HA - CD44	HAS2-HA-ligand	Undefined	CD44	P16070	PMID: 24406795 ; PMID: 31276783 ; PMID: 18661346
HAS2-HA - HMMR	HAS2-HA-ligand	Undefined	HMMR	O75330	PMID: 31276783 ; PMID: 24668563 ; PMID: 30365189
HAS2-HA - ICAM1	HAS2-HA-ligand	Undefined	ICAM1	P05362	PMID: 16449361 ; PMID: 8867647
HAS2-HA - TLR4	HAS2-HA-ligand	Undefined	TLR4	O00206	PMID: 21248167 ; PMID: 31484704
HAS2-HA - TLR2	HAS2-HA-ligand	Undefined	TLR2	O60603	PMID: 21248167 ; PMID: 28682809 ; PMID: 20534434
HAS2-HA - LYVE1	HAS2-HA-ligand	Undefined	LYVE1	Q9Y5Y7	PMID: 12554094 ; PMID: 19033446 ; PMID: 30054204
HAS3-HA - CD44	HAS3-HA-ligand	Undefined	CD44	P16070	PMID: 24406795 ; PMID: 31276783 ; PMID: 18661346
HAS3-HA - HMMR	HAS3-HA-ligand	Undefined	HMMR	O75330	PMID: 31276783 ; PMID: 24668563 ; PMID: 30365189
HAS3-HA - ICAM1	HAS3-HA-ligand	Undefined	ICAM1	P05362	PMID: 16449361 ; PMID: 8867647
HAS3-HA - TLR4	HAS3-HA-ligand	Undefined	TLR4	O00206	PMID: 21248167 ; PMID: 31484704
HAS3-HA - TLR2	HAS3-HA-ligand	Undefined	TLR2	O60603	PMID: 21248167 ; PMID: 28682809 ; PMID: 20534434
HAS3-HA - LYVE1	HAS3-HA-ligand	Undefined	LYVE1	Q9Y5Y7	PMID: 12554094 ; PMID: 19033446 ; PMID: 30054204

SUPPLEMENTARY METHODS

RNA isolation and real-time qPCR

Total tissue and cell RNA was isolated using TRIZOL and Tissue RNA isolation kit (Roche or Qiagen). RNA (1 μg) was reverse transcribed using TaqMan Reverse transcription reagent kit (Roche). Primers were designed in conjunction with the appropriate ABI probes (Applied Biosystems) and the samples were then used for real-time qPCR performed on PCR on Applied Biosystems™ QuantStudio™ 5 Real-Time PCR System (Applied Biosystems). Absolute values were quantified using relative standard curves, normalized to 18s expression and fold inductions were carried out with respect to livers of Naïve mice.

Bulk RNA sequencing

RNA from ultrapure HSC-CAF and quiescent samples was extracted using the RNeasy Micro or Mini Kit (Qiagen) with on-column DNAse digestion accordingly to manufacturer instructions. RNA (RNA integrity number [RIN] >8, as determined by Bioanalyzer 2100, Agilent Technologies) was used to construct libraries using Illumina TruSeq RNA Preparation Kit according to the manufacturer's instructions. 20M paired-end 100bp sequencing was performed using the Illumina NovaSeq 6000 at Columbia Genome Center. RTA (Illumina) was used for base calling and bcl2fastq2 (version 2.19) for converting BCL to fastq format, coupled with adaptor trimming. A pseudoalignment to a kallisto index was created from transcriptomes (Human: GRCh38; Mouse: GRCm38) using kallisto (0.44.0). Differentially expressed genes were tested using DESeq2. Normalization was done internally using DESeq2's specialized algorithm and

normalization to compare across samples, was performed using the TPM (transcripts per million) method.

Single-cell RNA sequencing

Murine single-cell RNA-seq was performed on cells isolated from mice withPan02 and CMT 93 liver metastasis as described below. Single-cell RNA-seq data from human CRC liver metastasis (***1***) and NET (***2***) have been previously published. CAF-enriched but multiple cell populations from Pan02 and CMT93 were obtained following the isolation protocol described above for CAF from Lrat-Cre+ TdTom+ Col1a1-GFP+ mice. In order to obtain CAF-enriched samples along with several other cell populations for CellPhoneDB analysis, we combined Col1a1-GFP+ cells (70%) with the unpurified live cell suspension (30%) by sorting on a BD Aria II Cell Sorter. Mouse tumor specimens were processed as previously described and freshly isolated cells were counted on Countess II automated cell counter (ThermoFisher) and were loaded on a 10x Chromium instrument (10x Genomics). Single-cell RNA-seq libraries were prepared using the Chromium Single Cell 3′ v3 Reagent Kit (10x Genomics) according to manufacturer's instructions. 12 cycles of cDNA amplification and 12 cycles of library amplification were performed, and samples were sequenced on an Illumina NovaSeq 6000 Sequencing System at the JP Sulzberger Columbia Genome Center. 10x Genomics Cellranger pipeline was used to process the data. BCL files were demultiplexed with 10x Cell Ranger's mkfastq command and analysis and alignment were performed using Cell Ranger's count command with Cell Ranger's reference mm10. Single-cell count matrices for both mouse and the human samples, were loaded into scanpy AnnData objects (scanpy v1.4.6). QC metrics (total number of counts, number of genes detected, percentage of mitochondrial RNA) was used to identify and remove outliers in the distribution of cells, cells with

high mitochondrial content (>40%) were excluded (***3***). Each cell was normalized using pool-derived size factors (***4***) and log-transformed each matrix. Principal component analysis was performed on the resulting matrices (scanpy v1.4.6). To identify cell sub-populations, we employed the Louvain algorithm for community detection (***5***) with different values for the resolution parameter, analyzing the average Silhouette score across all cells for each clustering (***6***). Differentially expressed genes were computed using the Wilcoxon Rank-Sum test as implemented in scanpy, and the different populations were labeled based on the genes differentially up-regulated in each population. Cell populations including CAF, hepatocytes, T and B lymphocytes, dendritic cells, endothelial cells, myeloid cells, monocytes and neutrophils, were identified using specific markers genes (Table S1) and confirmed by PanglaoDB (***7***). Mouse scores for panCAF and CAF subpopulations signatures were computed as previously defined (***8***). Clusters having at least 50% of cells with positive pan-CAF score were considered further for analysis of CAF subtypes. HSC-CAF and PF-CAF scores were calculated using the HSC and PF signatures in Table S1 and percentages were calculated for each sample. For mouse signatures, within panCAF, CAF subpopulation score distributions were analyzed, and a CAF subpopulation label was assigned to each cell if the corresponding score was higher than 0.125 (to reduce the number of cells with multiple labels). A signature for different CAF subpopulations by selecting differentially expressed genes between the different subpopulations ($q < 0.05$, log-FC > 1) was computed on single-CAF for each sample and 3 different populations were identified and named as iCAF, myCAF and mesCAF accordingly to their DGE and pathways enrichment as described in Results. The gene signature was analyzed in all cell populations to ensure the signature was specific to the particular CAF subset. Human panCAF and CAF subpopulation signatures were identified in "Human CRC metastasis and Human NET metastasis" datasets using the following procedure.

Literature-defined CAF signatures (*8*) and the mouse CAF signatures were used to define the cell clusters corresponding to panCAF and CAF subpopulations. panCAF signature was computed by obtaining the differentially expressed genes ($q < 0.05$, log-FC > 1) in PAN-CAF cluster compared to all other cell types and manually selecting genes with panCAF specific expression. HSC-CAF and PF-CAF were determined as previously described and CAF subpopulations iCAF, myCAF and mesCAF signatures were computed by obtaining the differentially expressed genes ($q < 0.05$, log-FC > 1) in the respective CAF subpopulation compared to the rest of panCAF and were independently validated by their differential gene expression and GO enrichment analysis (iCAF, myCAF and mesCAF human signatures are shown in Extended Data Table S1). These panCAF and CAF subpopulation signatures were then reapplied to the human sample to obtain and quantify CAF populations as mentioned previously. Notably, no mesCAF population was detected in the human samples.

CellPhoneDB Analysis

CellPhoneDB (*9*), a curated repository of ligands, receptors, their subunit interactions was used to identify ligand-receptor interactions in the three mouse models and human liver metastasis single cell RNAseq samples. Following identification of different cell types in our scRNA-seq datasets as described above, we followed recommended protocols for preparation of input files using CellPhoneDB v.2.0.0 (*9*). We updated the original CellPhoneDB repository with 43 novel interactions and 3 complexes curated from literature using 'cellphonedb database generate' command (Extended Data Table S3 provides Pubmed IDs with literature documenting the added interactions). All CellPhoneDB statistical analysis were performed with a percentage cell expression threshold of 1%. Cell-cell interactions heatmaps were generated using pheatmap R

package and ligand-receptor interactions were visualized using ggplot2 R package. Top common ligand receptor pairs between HSC-CAF and tumor cells were sorted based on significant means (p value <0.05) shown in Extended Data Table S4.

Rheometry

Tumor samples were extracted from liver specimens using a stainless-steel punch when >8mm, and cylindrical samples were cut manually and the diameter was determined from optical images. Parallel plate shear rheometry was carried out using a Kinexus rheometer (Malvern Panalytical, Westborough, MA). Samples were attached to the top and bottom plates with fibrin glue made by mixing 10 µl of 5 mg/ml salmon fibrinogen and 10 µl of 150 U/ml salmon thrombin (Sea Run Holdings, Freeport, ME) for each side of the sample. The top plate (8 mm diameter) was lowered until contact was made as determined by the application of 400 Pa normal stress, and the sample was allowed to rest for 5 min to ensure attachment to the metal plates. Shear storage modulus G', loss modulus G", and normal force were measured by applying a low oscillatory shear strain of 2% at a frequency of 1 rad/sec at room temperature. Simultaneously, samples were subjected to small stepwise axial strains in tension (0, 10, and 20%) followed by compression (-10, -15, -20, and -25%), between which the samples were allowed to relax for 2 min. The equilibrium G' and G" after 2 min of relaxation were plotted against axial strain.

Samples were always kept moist during experiments using PBS.

SUPPLEMENTARY REFERENCES

1. Y. Zhang, J. Song, Z. Zhao, M. Yang, M. Chen, C. Liu, J. Ji, D. Zhu, Single-cell transcriptome analysis reveals tumor immune microenvironment heterogenicity and granulocytes enrichment in colorectal cancer liver metastases. *Cancer Lett* **470**, 84-94 (2020).
2. M. Rao, K. Oh, R. Moffitt, P. Thompson, J. Li, J. Liu, A. Sasson, G. Georgakis, J. Kim, M. Choi, S. Powers, Comparative single-cell RNA sequencing (scRNA-seq) reveals liver metastasis-specific targets in a patient with small intestinal neuroendocrine cancer. *Cold Spring Harb Mol Case Stud* **6**, (2020).
3. T. Ilicic, J. K. Kim, A. A. Kolodziejczyk, F. O. Bagger, D. J. McCarthy, J. C. Marioni, S. A. Teichmann, Classification of low quality cells from single-cell RNA-seq data. *Genome Biol* **17**, 29 (2016).
4. A. T. Lun, K. Bach, J. C. Marioni, Pooling across cells to normalize single-cell RNA sequencing data with many zero counts. *Genome Biol* **17**, 75 (2016).
5. G. J.-L. Blondel VD, Lambiotte R, Lefebvre E. , Fast unfolding of communities in large networks. *J. Stat. Mech. Theory Exp.* **10008:6**, (2008).
6. P. J. Rousseeuw, Silhouettes: a graphical aid to the interpretation and validation of cluster analysis. *Journal of computational and applied mathematics* **20 (1987): 53-65**, (1987).
7. L.-M. G. a. J. L. M. B. r. Oscar Franzén, PanglaoDB: a web server for exploration of mouse and human single-cell RNA sequencing data. *Database* **2019, 1–9**, (2019).
8. E. Elyada, M. Bolisetty, P. Laise, W. F. Flynn, E. T. Courtois, R. A. Burkhart, J. A. Teinor, P. Belleau, G. Biffi, M. S. Lucito, S. Sivajothi, T. D. Armstrong, D. D. Engle, K. H. Yu, Y. Hao, C. L. Wolfgang, Y. Park, J. Preall, E. M. Jaffee, A. Califano, P. Robson, D. A. Tuveson, Cross-Species Single-Cell Analysis of Pancreatic Ductal Adenocarcinoma Reveals Antigen-Presenting Cancer-Associated Fibroblasts. *Cancer Discov* **9**, 1102-1123 (2019).
9. R. Vento-Tormo, M. Efremova, R. A. Botting, M. Y. Turco, M. Vento-Tormo, K. B. Meyer, J. E. Park, E. Stephenson, K. Polanski, A. Goncalves, L. Gardner, S. Holmqvist, J. Henriksson, A. Zou, A. M. Sharkey, B. Millar, B. Innes, L. Wood, A. Wilbrey-Clark, R. P. Payne, M. A. Ivarsson, S. Lisgo, A. Filby, D. H. Rowitch, J. N. Bulmer, G. J. Wright, M. J. T. Stubbington, M. Haniffa, A. Moffett, S. A. Teichmann, Single-cell reconstruction of the early maternal-fetal interface in humans. *Nature* **563**, 347-353 (2018).